since it appeared to best collapse the data. For the different sets of measurements, the ratio u_∞/u_τ is given to indicate what differences scaling by u_τ would have. As shown by Fig. 3, the results of the present study are strikingly similar to the incompressible results of Klebanoff. The turbulence intensity was not observed to level off in the inner part of the boundary layer as did Kistler's measurements.

Plotted in Fig. 4 are the Reynolds stress, $\rho u'v'$, results in an appropriately nondimensionalized form (the density ratio, ρ/ρ_∞ was calculated from pitot-tube data, assuming constant total temperature) and the wall shear stress as determined from Preston tube data. Apparent from this figure is the general agreement in the Reynolds shear stress in the inner portion of the boundary layer and the wall shear stress as would be expected for a zero pressure gradient boundary layer. The scatter in the Reynolds stress measurements can be attributed to the combined effect of a limited number of data samples and the differencing of two relatively large numbers. Values of $\overline{u'v'}$ for y/δ less than 0.15 are not reported since the lower frequency cutoff of the AEDC processing unit prevented the acceptance of all data within $3\langle V'\rangle$ of the mean at these locations.

IV. Conclusions

In this Note, measurements taken in a Mach 2.9 turbulent boundary layer are presented that demonstrate the ability of the laser velocimeter to measure the turbulence transport properties of high-speed compressible flows. This demonstrated ability combined with the nonperturbing quality and relative insensitivity to environmental conditions of the laser velocimeter open the way to compressible flow measurements never considered possible with more conventional measurement techniques.

References

[1] Van Driest, E. R., "Turbulent Boundary Layer in Compressible Fluids," *Journal of the Aeronautical Sciences*, Vol. 18, No. 3, March 1951, pp. 145–160.

[2] Morkovin, M. V., "Effects of Compressibility on Turbulent Flows," *The Mechanics of Turbulence*, Gordon and Breach, New York, 1964, pp. 367–380.

[3] Laufer, J., *Thoughts on Compressible Turbulent Boundary Layers*, NASA SP-216, Dec. 1968.

[4] Reda, R. C. and Murphy, J. D., "Shock Wave/Turbulent Boundary-Layer Interactions in Rectangular Channels," *AIAA Journal*, Vol. 11, No. 2, Feb. 1973, pp. 139–140.

[5] Logan, S. E., "A Laser Velocimeter for Reynolds Stress and Other Turbulence Measurements," *AIAA Journal*, Vol. 10, No. 7, July 1972, pp. 933–935.

[6] Yanta, W. J. and Smith, R. A., "Measurements of Turbulence-Transport Properties with a Laser Doppler Velocimeter," AIAA Paper 73-169, Washington, D.C., 1973.

[7] Lennert, A. E., Hornkohl, J. O., and Kalb, H. T., "Applications of Laser Velocimeters for Flow Measurements," *Proceedings of the Air Breathing Propulsion Conference*, Monterey, Calif., Sept. 1972.

[8] Klebanoff, D. S., "Characteristics of Turbulence in a Boundary Layer with Zero Pressure Gradient," Rept. 1247, 1955, NACA.

[9] Johnson, D. A., "Insensitivity of Single Particle Time Domain Measurements to Laser Velocimeter 'Doppler Ambiguity'," *AIAA Journal*, Vol. 11, No. 6, June 1973, pp. 890–892.

[10] Green, H. L. and Lane, W. R., *Particulate Clouds: Dusts, Smokes and Mists*, Van Nostrand, Princeton, N.J., 1964.

[11] Yanta, W. J. and Gates, D. F., "The Use of a Laser Doppler Velocimeter in Supersonic Flow," AIAA Paper 71-287, Albuquerque, N.Mex., 1971.

[12] Owen, F. K. and Horstman, C. C., "On the Structure of Hypersonic Turbulent Boundary Layers," *Journal of Fluid Mechanics*, Vol. 53, Pt. 4, 1972, pp. 611–636.

[13] Allen, J. M., "Pitot-Probe Displacement in a Supersonic Turbulent Boundary Layer," TN D-6759, 1972, NASA.

[14] Rose, W. C., "Turbulence Measurements in a Compressible Boundary Layer Subjected to a Shock-Wave-Induced Adverse Pressure Gradient," AIAA Paper 73-167, Washington, D.C., 1973.

[15] Kistler, A. L., "Fluctuation Measurements in a Supersonic Boundary Layer," *Physics of Fluids*, Vol. 2, No. 3, May–June 1959, pp. 290–296.

Shell Instability Analysis Applied to a Radome

TERRY L. JANSSEN* AND THOMAS G. SWANEY†

The Boeing Company, Wichita, Kansas

Introduction

In the instability analysis of shells, a bifurcation buckling analysis is the easiest and least expensive. A bifurcation point defines a load level at and above which some new deformation mode is possible. The bifurcation buckling analysis is based on the classical approach of solving a linear eigenvalue problem. The lowest eigenvalue, denoted as the classical buckling load, represents a prestressed state at which another equilibrium state is possible. The uncertainty of the classical buckling load for arbitrary shells is well known.[1,2] It is clear from experimental results that more than the knowledge of the classical buckling load and its corresponding mode shape is required to yield the load at which an arbitrary shell will collapse. For a general shell, if the shell geometry deteriorates appreciably or stresses are redistributed in the subcritical load range, failure usually occurs by means of collapse at a limit point rather than through bifurcation.

Theory

In the theory of elasticity, geometric nonlinearity is introduced from two sources: the strain-displacement equations and the equilibrium equations. In the finite element technique, the nonlinear strain-displacement relationships are recognized through the use of the differential stiffness matrix, also called the geometric or initial stress stiffness matrix. This matrix is added to the linear stiffness matrix and is a function of the elemental internal loads. The nonlinear equilibrium equations are recognized by using an incremental step procedure. The actual deformed geometry is taken into account at the start of each step.

To demonstrate the manner in which the finite element method satisfies the nonlinear strain-displacement relationships it is convenient to separate the strain energy into two parts

$$U = U_L + U_{NL} \tag{1}$$

U_L is due to the linear strain displacement terms. U_{NL} is due to the nonlinear terms caused by rotation of the element. The

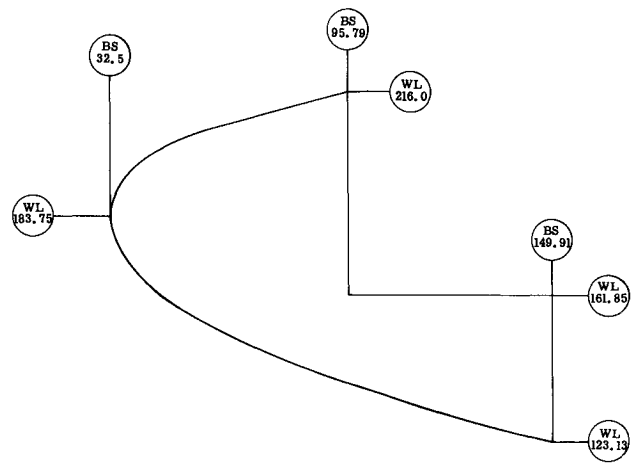

Fig. 1 Structural side view.

Received August 2, 1973.

Index categories: Aircraft Structural Design (Including Loads); Structural Stability Analysis; Structural Static Analysis.

* Senior Engineer, Structures Staff.

† Senior Group Engineer, Structures Staff.

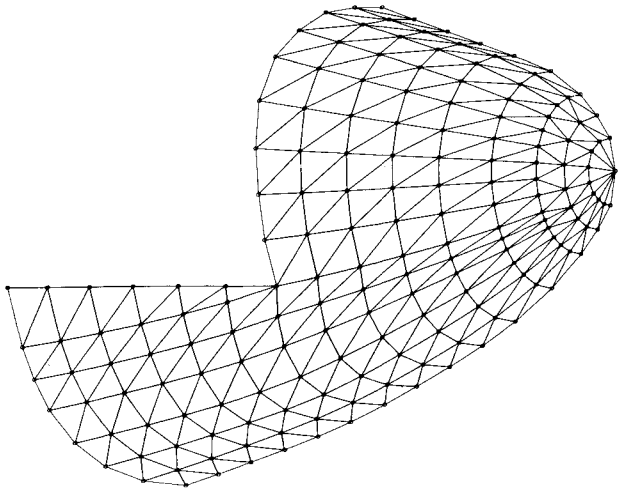

Fig. 2 Finite element idealization.

strain energy is generally written in terms of the nodal displacements u_i. An application of Castigliano's first theorem gives the stiffness coefficient $[K_{ij}]$ as

$$[K_{ij}] = \frac{\partial^2 U}{\partial u_i \partial u_j} = \frac{\partial^2 U_L}{\partial u_i \partial u_j} + \frac{\partial^2 U_{NL}}{\partial u_i \partial u_j} = [K] + [K^*] \quad (2)$$

$[K]$ is the conventional elastic stiffness matrix and $[K^*]$ is denoted as the geometric stiffness matrix. Thus, the complete equilibrium equation is

$$\{F\} = ([K] + [K^*])\{u\} \quad (3)$$

Przemieniecki[3] shows that a solution to the classical bifurcation buckling problem can be obtained by the following equation:

$$|[K] + \lambda[K^*]| = 0 \quad (4)$$

This is the standard eigenvalue problem where the minimum eigenvalue, λ_{min}, represents the buckling load.

A solution to the geometric nonlinear problem is obtained by a piecewise linear approach called the incremental step procedure. The method assumes that a solution of Eq. (3), $\{u_o\}$, is known at some load $\{F_o\}$. It is then desired to find a solution $\{u_o + \Delta u\}$ at some loading $\{F_o + \Delta F\}$. Thus, Eq. (3) yields

$$[K][\{u_o\} + \{\Delta u\}] + [K^*][\{u_o\} + \{\Delta u\}] = \{F_o\} + \{\Delta F\} \quad (5)$$

or

$$[[K] + [K^*]]\{\Delta u\} = \{\Delta F\} + \{F_o\} - [[K] + [K^*]]\{u_o\} \quad (6)$$

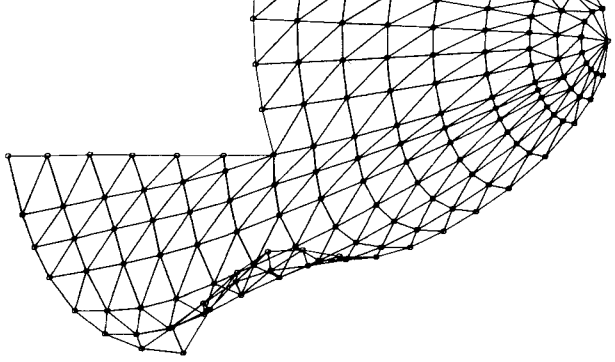

Fig. 3 Bifurcation buckling mode shape.

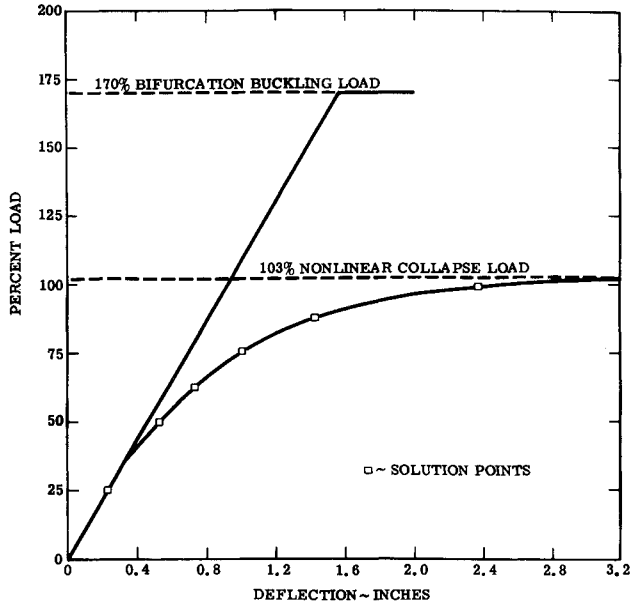

Fig. 4 Typical load-deflection curve.

However, the last two terms in Eq. (6) represent the equilibrium equation and are equal to zero for a true equilibrium position $\{u_o\}$. Thus, the equation for determining the incremental displacements is given by

$$\{\Delta u\} = [[K] + [K^*]]^{-1}\{\Delta F\} \quad (7)$$

For small strains, lengths in $[K]$ can be taken as the values prior to any deformation. For $[K^*]$, lengths should be taken as the values in effect at the beginning of each step. For both $[K]$ and $[K^*]$, the elemental direction cosines are the values existing at the beginning of each step. This is essentially the procedure by Martin.[4]

Radome Model

The previously defined finite element techniques were applied to the nose radome of a large aircraft. A sideview of the radome is shown in Fig. 1. The geometric idealization of the radome consisted of one structurally symmetric half defined by a vertical plane on the centerline of the airplane. A computer-generated plot of the model idealization is shown in Fig. 2. The mesh contains 179 nodes with 310 triangular plate and 7 beam elements. Constraints on the model consisted of symmetry constraints along the plane of symmetry and constraints to simulate the latch points on the aft face of the radome. Loads consisted of a nonuniform collapsing pressure distribution.

The radome is constructed of a uniform sandwich-type arrangement of orthotropic fiberglass material. A plate element developed for sandwich construction was utilized. This plate element considered the orthotropic material properties of the face sheets and the transverse shear flexibility of the core. The material properties were obtained experimentally for the specific material used in fabricating the radome.

Results and Discussion

Utilizing Eq. (4), a solution for the classical bifurcation buckling load was obtained. The predicted instability was at a load value of 170% of the total applied loads. A computer-generated plot of the buckled mode shape is shown in Fig. 3. A geometric nonlinear solution using Eq. (7) in a nine-step incremental solution was then performed. A typical load-deflection plot for a point on the lower centerline of the radome is shown in Fig. 4. This analysis predicted a large deflection collapse at a 103% load value. A static test of the actual radome

showed a large deflection collapse in the predicted area at a 100% load value.

From the radome analysis results, it is observed that a large discrepancy exists between the bifurcation buckling and collapse loads. The primary reason is that considerable distortion of geometry occurs at loads below the predicted bifurcation buckling.

The finite element technique yielded excellent results for a complicated shell problem which included orthotropic sandwich-plate construction. The method is straightforward in use and general in application.

References

[1] Almroth, B. O. and Brogan, F. A., "Bifurcation Buckling as an Approximation of the Collapse Load for General Shells," *AIAA Journal*, Vol. 10, No. 4, April 1972, pp. 463–467.

[2] Bushnell, D. and Almroth, B. O., "Finite Difference Energy Method for Nonlinear Shell Analysis," *Proceedings of a Conference on Computer Oriented Analysis of Shell Structures*, AFFDL-TR-71-79, June 1971, Air Force Flight Dynamics Lab., Wright-Patterson Air Force Base, Ohio, pp. 337–390.

[3] Przemieniecki, J. S., *Theory of Matrix Structural Analysis*, 1st ed., McGraw-Hill, New York, 1968, pp. 383–386.

[4] Martin, H. C., "Large Deflection and Stability Analysis by the Direct Stiffness Method," TR-32-931, Aug. 1966, Jet Propulsion Lab., Pasadena, Calif.

Unsteady Temperature Distribution in Volume Reflectors

KENNETH C. WESTON* AND R. S. REDDY†
University of Tulsa, Tulsa, Okla.

FEW authors have considered the development of unsteady temperature distributions in semitransparent scattering materials under the influence of arbitrary incident radiative flux with other than specified temperature boundary conditions. The present work considers such a problem for an approximate radiative transfer model which allows analytic solutions. Such solutions are useful in the analysis of volume-reflecting heat shields considered for planetary entry environments in which incident radiative heating is dominant.[1] The model represents the unsteady, one-dimensional, radiative heating of a weakly absorbing, semitransparent medium with specified conductive heat flux at one boundary. The radiation field is modeled using an approximation[1] to the radiative heat flux obtained by solution of the Kubelka-Munk differential equations which have been successfully employed for many years in the paint and paper industry.[2,3] The radiation field in this model is characterized by two fluxes, a transmitted flux, I_T, and a reflected flux, I_R. It is assumed that internal radiative emission may be neglected with respect to the internally transmitted fluxes. This is justified for moderate temperatures and low absorption coefficients. The latter condition, of course, is necessary for a material to be a good volume reflector.[1] The index of refraction of the medium enveloping the scattering centers is assumed to be close to unity, eliminating the need for consideration of the surface reflectance at the boundaries of the slab.

Received September 17, 1973. This work was supported under NASA Grant NGR 37-008-003.

Index categories: Heat Conduction; Radiation and Radiative Heat Transfer; Thermal Modeling and Experimental Thermal Simulation.

* Associate Professor. Member AIAA.

† Graduate Research Assistant.

The Kubelka-Munk differential equations are

$$dI_T/dy = -(s+k)I_T + sI_R \tag{1a}$$

$$dI_R/dy = (s+k)I_R - sI_T \tag{1b}$$

where s and k are the Kubelka-Munk scattering and absorption coefficients and y is the coordinate measured normal to the boundary. Defining the radiative heat flux as

$$q_R = \pi(I_T - I_R) \tag{2}$$

subtraction of Eq. (1b) from Eq. (1a) leads to the following expression for the divergence of the radiative heat flux

$$dq_R/dy = -k\pi(I_T + I_R) \tag{3}$$

The radiative heat flux divergence may be expressed approximately in terms of scattering and absorption coefficients and position by solving Eqs. (1) simultaneously for I_T and I_R under the condition $k = 0$ and substituting into Eq. (3). Defining the arbitrary diffuse, incident, radiative flux q_0, and the over-all reflectance, R, the boundary conditions for the solutions of Eqs. (1) may be formulated as

$$I_T(0) = q_0/\pi,\ I_R(0)/I_T(0) = R \tag{4}$$

The solutions of Eqs. (1) with $k = 0$ which satisfy Eqs. (4) are found to be

$$I_T = q_0/\pi[1 - sy(1-R)] \tag{5a}$$

$$I_R = q_0/\pi[R - sy(1-R)] \tag{5b}$$

leading to the radiative heat flux divergence expression‡

$$dq_R/dy = -kq_0[R + 1 - 2sy(1-R)] \tag{6}$$

The reflectance R of a slab of semitransparent material of thickness δ is known from reflectance solutions of the Kubelka-Munk differential equations[1] as

$$R = \frac{(1/R_\infty)(R_B - R_\infty) - R_\infty(R_B - 1/R_\infty)\exp[S(1/R_\infty - R_\infty)]}{(R_B - R_\infty) - (R_B - 1/R_\infty)\exp[S(1/R_\infty - R_\infty)]} \tag{7}$$

where

$$R_\infty = 1 + k/s - [k/s(k/s+2)]^{1/2} \tag{8}$$

Here R_∞ is the reflectance of an infinite thickness of the media, $S = s\delta$ is the scattering power of the media for the thickness δ, and R_B is the rear surface reflectance. Equations (6–8) thus determine the interaction of the radiation and temperature fields through the radiative flux divergence for assigned values of k, s, δ, R_B, and q_0.

The temperature field is governed by the energy equation

$$\rho C\frac{\partial T}{\partial t} = K\frac{\partial^2 T}{\partial y^2} + q_0 k[1 + R - 2sy(1-R)] \tag{9}$$

where the source term is given by the radiative flux divergence in Eq. (6). It is convenient to define the following dimensionless parameters:

$$\tau = \alpha t/\delta^2, \quad \eta = y/\delta, \quad \theta = T/T_s, \quad \Phi = kq_0\delta^2/KT_s$$

which transform Eq. (9) into

$$\partial\theta/\partial\tau = \partial^2\theta/\partial\eta^2 + \Phi[1 + R - 2S(1-R)\eta] \tag{10}$$

Equation (10), together with appropriate initial and boundary conditions, provides an initial-boundary value problem for the determination of $\theta(\eta, \tau)$.

We restrict our consideration to the class of solutions in which the initial temperature is constant and the rear surface is a perfect insulator which transmits all incident unreflected radiation. Specifying the constant, dimensionless temperature gradient at the surface $y = 0$ as A, the initial and boundary conditions are

$$\theta(\eta, 0) = \theta_1, \qquad 0 < \eta < 1 \tag{11}$$

$$\theta_\eta(0, \tau) = A, \qquad \theta_\eta(1, \tau) = 0, \qquad \tau > 0 \tag{12a, b}$$

‡ Note that Eqs. (2–5) here differ from the corresponding equations given in Ref. 1. In that reference, the factors of π are absent. This difference exists because here the symbols I_T and I_R are considered to be radiant intensities, whereas in Ref. 1, they were regarded as half-fluxes. It should be noted that the π factors drop out of the analysis at this point leading to the same radiative heat flux divergence and energy equations as those found in the reference.